

## Organic matter on the Earth's Moon

Kathie L. Thomas-Keprta<sup>a,\*</sup>, Simon J. Clemett<sup>a</sup>, Scott Messenger<sup>b</sup>,  
Daniel K. Ross<sup>a</sup>, Loan Le<sup>a</sup>, Zia Rahman<sup>a</sup>, David S. McKay<sup>b,1</sup>,  
Everett K. Gibson Jr.<sup>b</sup>, Carla Gonzalez<sup>a</sup>, William Peabody<sup>c</sup>

<sup>a</sup> *Jacobs JETS, NASA Johnson Space Center, Mail Code KR, Building 31, Houston, TX 77058, United States*

<sup>b</sup> *NASA Johnson Space Center, KR, Houston, TX 77058, United States*

<sup>c</sup> *Keyence, Micro-Analysis Group, 18111 Preston Rd. Suite 210, Dallas, TX 75252, United States*

Received 2 September 2013; accepted in revised form 21 February 2014; available online 15 March 2014

### Abstract

Carbonaceous matter on the surfaces of black pyroclastic beads, collected from Shorty crater during the Apollo 17 mission, represents the first identification of complex organic material associated with any lunar sample. We report the chemical, physical and isotopic properties of this organic matter that together support a pre-terrestrial origin. We suggest the most probable source is through the accretion of exogenous meteoritic kerogen from micrometeorite impacts into the lunar regolith. Abiotic organic matter has been continuously delivered to the surfaces of the terrestrial planets and their moons by accretion of asteroidal and cometary material. Determining the nature, distribution and evolution of such matter in the lunar regolith has important implications for understanding the prebiotic chemical inventory of the terrestrial planets. © 2014 Elsevier Ltd. All rights reserved.

### 1. INTRODUCTION

After more than 40 years of research, there has been no conclusive identification of indigenous organic matter in any of the Apollo lunar samples, with the exception of methane (CH<sub>4</sub>) (Burlingame et al., 1970; Ponnampetuma et al., 1970; Preti et al., 1971; Gehrke et al., 1973). We report here, for the first time, the identification of arguably lunar organic matter, as thin surface coatings, on pyroclastic black glass beads collected on the rim of Shorty crater by Apollo 17 astronauts Eugene Cernan and Harrison Schmitt.

In the buildup to the Apollo Moon landings, there was much speculation, most prominently by Gilvarry (1960)

and Sagan (1960, 1961), as to whether indigenous organic matter would be found in the lunar regolith. The former postulated the presence of organic remains derived from a pristine biota in a hydrosphere formed by exudation from the Moon's interior and lasting several billion years; while, the latter postulated the synthesis of organic molecules through the action of ionizing radiation in a primordial lunar atmosphere of CH<sub>4</sub>, ammonia (NH<sub>3</sub>) and water-vapor (H<sub>2</sub>O). Sagan (1961) surmised “*The overall deposition of organic matter after the Moon's formation may well have been as great as 10 gm cm<sup>-2</sup>.*” It therefore came as a surprise when the first organic chemistry results from the Apollo 11 lunar samples, presented in ‘*The Moon Issue*’ of *Science* (January 30, 1970), revealed unexpectedly low carbon (C) abundances and no evidence of any indigenous organics. A later review of bulk lunar soils from all the Apollo missions gives an average C abundance of 124 ± 45 ppm (Fegley and Swindle, 1993).

In the post-Apollo era, the absence of organic matter in the lunar regolith remains enigmatic. A substantial

\* Corresponding author. Tel.: +1 2814835029; fax: +1 2814831573.

E-mail address: [kathie.thomas-keprta-1@nasa.gov](mailto:kathie.thomas-keprta-1@nasa.gov) (K.L. Thomas-Keprta).

<sup>1</sup> Deceased.

contribution to the abiotic organic inventory of the early Earth is thought to have come from accretion of comets and asteroids (Anders, 1989; Chyba and Sagan, 1992), predominately in the form of C-rich micrometeorites and interplanetary dust particles (IDPs) (Flynn et al., 2000). Consequently, the same process should contribute to the organic inventory of the lunar regolith. Uncertainty of the density and composition of the Moon's early atmosphere, however, limits our ability to estimate the degree of exogenous organic matter preserved in the lunar regolith. For example the density of the putative lunar atmosphere would influence the survival organic matter during accretion, while its oxidation state would impact the thermodynamic stability of accreted material.

## 2. SAMPLE HISTORY AND BACKGROUND

*"... It's orange... Sure it is... Crazy! I've got to dig a trench, Houston."* H. Schmitt to E. Cernan

On December 13, 1972 sample 74220,0, weighing 1180 g, was collected from Station 4 at the rim crest of Shorty crater by Apollo 17 astronaut Harrison Schmitt. The sample, a clod of orange-tinted friable material, was placed in lunar sample bag #509, composed of Teflon<sup>®</sup> film. On December 27, 1972, in the NASA Johnson Space Center (JSC) Lunar Curatorial Facility subsample 74220,1 was listed as reserve and placed in a stainless steel acid-washed bolt top can (1B-201). On February 2, 1973, February 9, 1973 and again on February 13, 1973, the container was opened and splits were produced from 74220,1. On February 14, 1973 74220,1 was opened and split 74220,92, weighing 100 g, was placed into a slide-lid container which was then double sealed in two 2-ml thick Teflon<sup>®</sup> bags. The bagged slide-lid can was bolted into a Radiation Counting Container sealed with an O-ring and bagged with one 2-ml Teflon<sup>®</sup> bag. On May 21, 1973 sample 74220,92 was scooped with a stainless steel tool into a bolt-top container (1B-42). On September 12, 1974 sample 74220,174 was removed from sample 74220,92. On November 14, 1974 74220,92 was transferred to remote storage in a vault in Building 45 at NASA JSC. After 74220,92 was returned to the Pristine Laboratory, it was transferred in a bolt-top container to the GN<sub>2</sub> cabinet in the Experimental Laboratory in order to remove the soil from the bolt-top because the bolt had Xylan lubricant on the threads. The soil was then transferred into a screw-top can with a 2-ml Teflon<sup>®</sup> gasket (82-51) on January 20, 1993. The sample 74220,92 was split again on December 2, 1997 and on April 28, 1998. In April 1998, a subsample 74220,805 was produced from 74220,92 and was transferred to a stainless steel Teflon<sup>®</sup> pop-top canister (9-12320). Finally, on September 20, 2007 a subsample of 74220,805 was transferred to a stainless steel Teflon<sup>®</sup> pop-top container (9-9189) to become sample 74220,861. The pop-top canister was purged with dry N<sub>2</sub> and enclosed within two heat sealed Teflon<sup>®</sup> bags before being allocated to D. S. McKay for analysis. At no time during the curation process was the sample sieved, and all sample subdivisions were conducted in positive pressure stainless steel glove boxes under dry N<sub>2</sub>. Allocation 74220,861 was opened for

the first time under dry N<sub>2</sub> in April of 2012 to retrieve the glass beads used in this study. Because the chain of custody for allocation 74220,861 remains unbroken and is well documented, there has been no opportunity for any organic contamination since its removal from the rim of Shorty crater.

Sample 74220,861 is composed predominantly of orange and devitrified black 'glass' beads ranging from one to several hundred microns in diameter produced in a fire fountain eruption presumably driven by the expansion of carbon dioxide (CO<sub>2</sub>) gas produced by the oxidation of graphite in the magma (Heiken et al., 1974; Meyer et al., 1975; Heiken and McKay, 1977). Because the bulk composition of comparable beads from a 67 cm long double drive tube (core sample 74001/74002), collected near the trench at Shorty crater (Blanchard and Budahn, 1978) does not change with core depth, all the pyroclastic beads are believed to have formed in a single eruption. Accounting for the inversion of the original stratigraphy of core sample 74001/2, due to the impact that formed Shorty, the deposition sequence began with predominantly orange glasses that evolved to black glasses. This transformation reflects both a change in the cooling rate of the glasses and the gas content of the fire fountain (Weitz et al., 1997). The beads have radiogenic crystallization ages ranging from ~3.66 Ga (Alexander et al., 1980) to ~3.60 Ga (Huneke, 1978), based on <sup>40</sup>Ar/<sup>39</sup>Ar measurements and formed in the cooling ejecta of a fire fountain eruption (Weitz et al., 1997). The cosmic ray exposure age, *i.e.*, the time spent in the upper few centimeters of regolith, range from ~10 Ma (presumed age of Shorty) to 35 Ma ago (Kirsten et al., 1973; Fleischer et al., 1974; Eugster et al., 1977; Crozaz, 1979). This exposure is thought to have occurred in two stages: (1) an initial exposure of ~20 Ma following formation and before burial in the regolith; and, (2) a secondary exposure due to excavation by the impact that formed Shorty (Bogard and Hirsch, 1978). Textural differences between the orange and black beads are also attributed to differing cooling rates (Arndt and Engelhardt, 1986); the orange beads cooled rapidly enough to inhibit crystal formation, whereas the black beads cooled more slowly leading to formation of finely feathered crystals of ilmenite embedded in a matrix of olivine and/or glass.

## 3. METHODS

### 3.1. Sample preparation and mounting

Orange and black lunar glass beads were selected at random from our sample allocation 74220,861. Each bead was transferred using stainless steel surgical tweezers to an Al planchet positioned on a custom built heating platform, attached to the stage of a stereo binocular microscope. In order to anchor the glass beads to the Al planchet the thermal polymer CrystalBond™ 509 was used as an adhesive, a small grain (~10–20 μm in size) being allowed to soften to a semi-liquid state on the planchet prior to the transfer of a glass bead. By placing a glass bead on the top of the viscous CrystalBond™ droplet and then removing the planchet from the heating stage, the CrystalBond™ immediately

solidified firmly attaching the glass bead to the planchet. We have established that this mounting procedure produces no detectable sample contamination and is vacuum chamber compatible.

### 3.2. Analytical methods

Prior to sample mounting, black beads were first examined optically and for native ultraviolet (UV) fluorescence to identify candidate C-bearing regions of interest (ROIs). Selected grains with ROIs were subsequently mounted and investigated by  $\mu$ -Raman spectroscopy and two-step laser desorption/laser ionization mass spectrometry ( $\mu$ -L<sup>2</sup>MS) to determine the nature of organic phases present. Following this, field emission scanning electron microscopy (FESEM) in conjunction with light element energy dispersive X-ray spectrometry (EDX) was used to determine the textural and chemical composition of the ROIs. In one instance, focused ion beam (FIB) microscopy was then used to extract an electron transparent thin section for mineralogical and chemical characterization using field emission scanning transmission electron microscopy (FESTEM) and light element EDX. This section was subsequently analyzed using a NanoSIMS ion microprobe for C and N isotopic compositions.

#### 3.2.1. Optical microscopy/UV fluorescence imaging

For contextual documentation, glass beads were optically imaged using an Olympus BX60 optical/UV fluorescence microscope. Since the surface topography of the samples exceeded the imaging depth-of-field for a single focus position, a wavelet-based image processing technique (Forster et al., 2004) was used to create extended depth-of-field image mosaics from Z-focus image stacks and a seam line optimization algorithm was used for mosaic image compositing. In the case of one glass bead designated as #1, we also performed additional imaging using a Keyence VK-X200 3D laser scanning microscope.

UV fluorescence imaging, using a 330–385 nm excitation filter in combination with a 420 nm long pass emission filter, was then used to identify the location of potential carbonaceous phases. This is particularly effective at identifying aromatic species such as polycyclic aromatic hydrocarbons which exhibit a high intrinsic fluorescence because their rigid molecular structure does not allow for efficient vibrational relaxation.

#### 3.2.2. Raman spectroscopy

Raman spectroscopy was used as a secondary verification tool to confirm identification of carbonaceous matter, and as a probe of the state of structural organization of identified organic phases. While interpretation of Raman spectra can be difficult where multiple carbonaceous phases coexist in a single sample, it is nevertheless a valuable tool in determining the nature of C when used in conjunction with other techniques such as high resolution transmission electron microscope imaging. We used a Jobin–Yvon Horiba LabRAM HR 800  $\mu$ -Raman spectrometer operating at a probe spatial resolution of  $\sim 1 \mu\text{m}$  and equipped with an Ar laser operating at a wavelength of 514 nm, coupled to

Olympus BX 41 optical microscope. Under these conditions, the wavelength accuracy of the spectrometer was  $\pm 1 \text{ cm}^{-1}$  with a spectral resolution of  $\sim 0.5\text{--}1 \text{ cm}^{-1}$ . A Si calibration standard was used to ensure the correct calibration and linearity of the spectrograph prior to sample analyses and the lateral spatial resolution of the analysis spot on the sample was determined to be  $\sim 1 \mu\text{m}$ . Samples were scanned in multiple steps from 300 to 3000/3500  $\text{cm}^{-1}$ , and the laser power density was carefully controlled to avoid thermal damage. This was subsequently confirmed by using scanning electron microscopy to check for laser induced heating artifacts.

The most prominent features in the Raman spectra of graphitic materials are four peaks that, in deference the nomenclature of the early Raman literature, are known as the, D ( $\sim 1350 \text{ cm}^{-1}$ ), G ( $\sim 1580 \text{ cm}^{-1}$ ), D' ( $\sim 1620 \text{ cm}^{-1}$ ) and G' ( $\sim 2700 \text{ cm}^{-1}$ ) bands (Tuinstra and Koenig, 1970a,b; Reich and Thomsen, 2004). The G band corresponds to the first-order double degenerate in-plane  $E_{2g}$  vibration mode characteristic of all aromatic  $\text{sp}^2$  bonding carbon networks. In contrast, the D and D' bands are defect-induced features, which are absent in the Raman spectra of highly crystalline graphite (Ferrari and Robertson, 2000; Robertson, 2002). Consequently the intensity ratio of the D and G bands ( $I_D/I_G$ ) is a widely used parameter for characterizing the defect quantity in graphitic materials. In particular in the in-plane crystallite size ( $L_a$ ) of graphitic domains has been shown to vary inversely with  $I_D/I_G$  (Tuinstra and Koenig, 1970a,b). This has led to several empirical derived expressions to allow the determination of  $L_a$  from the  $I_D/I_G$  ratio (Knight and White, 1989; Beyssac et al., 2002; Muñoz Caro et al., 2006; Ferrari, 2007).

The D' band of carbonaceous materials with a high degree of disorder and/or small domain sizes can often overlap the G band. To simplify the later discussion of acquired Raman spectra and permit comparison with prior literature (Muñoz Caro et al., 2006; Busemann et al., 2007), we have not attempted to resolve these band overlaps. Consequently, in subsequent discussions of G band parameters, it should be realized we implicitly recognize a minor contribution to experimentally observed G band due to D' band overlap. Peak centers and the full width half-maximum of peaks in acquired spectra were determined by peak fitting to two Voigt distributions (convolution of a Lorentzian with a Gaussian profile) using a Levenberg–Marquardt optimization algorithm.<sup>2</sup>

#### 3.2.3. Two-step laser desorption/laser ionization mass spectrometry ( $\mu$ -L<sup>2</sup>MS)

The  $\mu$ -L<sup>2</sup>MS was used for the detection and identification of organic molecules in lunar samples. The JSC  $\mu$ -L<sup>2</sup>MS instrument is equipped with a vacuum ultraviolet (VUV) ionization source capable of non-resonant single-photon soft ionization enabling the *in situ* detection of virtually any organic molecular system at high sensitivity

<sup>2</sup> The D band was fit using a symmetric Voigt function, while the G band was fit with an asymmetric Voigt function, the latter being a consequence of the observed G band asymmetry due to D' band overlap.

(>10<sup>-18</sup> mol) and spatial resolution (~5 µm). The generation of coherent VUV radiation is achieved by the non-linear frequency tripling of the 3rd harmonic (λ 355 nm) of a mode-locked Q-switched picosecond Nd:YAG laser in a Xe–Ar gas cell to produce 118.2 nm (~10.5 eV) radiation (Lockyer and Vickerman, 1997; Shi and Lipson, 2005). Since the first ionization potentials for nearly all organic molecules lie in the range of 5–10 eV (King et al., 2003) effectively all organic species can be photoionized with 10.5 eV photons.

### 3.2.4. Electron/ion beam instrumentation

High resolution imaging and chemical analyses of *in situ* carbonaceous matter were performed using a JEOL 7600 field emission scanning electron microscope coupled with a Noran System 6 energy dispersive X-ray spectrometer. A Pt surface coating ~1 nm thick was applied to enable imaging and chemical characterization of elements including C at 10 and 15 kV. We extracted an electron transparent thin section from the largest C-rich ROI located on glass bead #1 using a FEI Quanta 3D Dual Beam FIB microscope (Zega and Stroud, 2006). The FIB section was analyzed using a JEOL 2500SE FETEM featuring a large area, thin window Noran System 6 EDX detector for imaging and element mapping down to a resolution of 10 nm. Imaging resolution in STEM and TEM modes are 0.2 and 0.14 nm, respectively.

The JSC NanoSIMS 50L was used to obtain C and N isotopic images of the FIB section extracted from ROI #1 located on bead #1. Images were obtained by rastering  $a < 100$  nm, 16 keV Cs<sup>+</sup> ion beam over a 15 × 15 µm field of view. Images of <sup>12</sup>C, <sup>13</sup>C, <sup>12</sup>C<sup>14</sup>N, <sup>12</sup>C<sup>15</sup>N, <sup>16</sup>O, <sup>28</sup>Si and <sup>16</sup>O<sup>24</sup>Mg secondary ions were collected simultaneously in multi-detection mode with electron multipliers. These images were repeatedly obtained for a total of 40 image frames over the field of view. The carbonaceous inclusions in the FIB section were clearly identifiable in the images by localized enhancements in <sup>12</sup>C<sup>14</sup>N<sup>-</sup> elemental ion signal. Some regions of the carbonaceous materials also exhibited significant <sup>16</sup>O<sup>-</sup> concentrations. The C and N isotopic measurements were normalized to terrestrial USGS graphite and 1-hydroxybenzotriazole hydrate, respectively. The data were corrected for instrumental mass fractionation, electron multiplier dead time, and quasi-simultaneous arrivals. Isotopic and elemental abundance ratios were determined for regions of interest within the images by custom software.

## 4. RESULTS

Three of the black glass beads we analyzed, designated as #1, #2, and #3, showed weakly fluorescing surface features, several µm<sup>2</sup> in size, consistent with emission from excited  $n \rightarrow \pi^*$  and  $\pi \rightarrow \pi^*$  states in aromatic and/or conjugated organic matter. This identification was subsequently confirmed by  $\mu$ -Raman and by mass spectrometry using  $\mu$ -L<sup>2</sup>MS. The largest of the ROIs measured ~4 × 7 µm and was located on a corner of a rectangular plateau situated upon the surface of glass bead #1 designated henceforth as ROI #1 (Figs. 1a and b). In this ROI, a Si-

rich finger-like projection extends up from the surface of the plateau and partially overlays the carbonaceous material (Fig. 1c), indicating the underlying organic material was already present when the siliceous phase was deposited. Because the elemental composition of this siliceous projection is indistinguishable from that of the plateau and represents a physical extension of the surface of the plateau, they share a common origin. This suggests two scenarios: in the first, the organic phase became attached to the surface of the glass bead shortly after its ejection from the fire-fountain eruption while the plateau material on which it sits was itself still molten or semi-molten. Alternatively, in the second, during the bead's later residence in the lunar regolith, the organic material formed and deposited during an impact driven event which was also able to locally melt the surface of the bead.

EDX mapping of ROI #1 show it is composed primarily of C that is heterogeneously distributed (Figs. 1d–g). The presence of localized concentrations of Al, Si, Ti and Fe (Fig. 1d) indicate glass and/or minerals grains up to ~400 nm in size are embedded within the carbonaceous phase. Grains enriched in Ti with minor Al are attributed to TiO<sub>2</sub>, which is usually present in the lunar regolith in the form of the polymorph rutile, although this was not confirmed by Raman or TEM. Similar grains containing minor Al (0.82 wt.%) have previously been reported in an Apollo 14 micro-breccia sample 14162,16 (Hlava et al., 1972), where the substitution of Al into TiO<sub>2</sub> can occur under high pressure conditions (Escudero et al., 2011). Grains composed of Fe and Ti are likely ilmenite (FeTiO<sub>3</sub>), while those composed primarily of Si and Al represent a glass.

Characterization of ROI #1 by  $\mu$ -Raman spectroscopy showed strong D and G bands and their associated second order bands (Table 1; Figs. 2a and b). The position of the G band center varied from 1578 to 1597 cm<sup>-1</sup> while its full-width at half-maximum (FWHM) ranged from 117 to 129 cm<sup>-1</sup>. Compared with the D band,  $I_D/I_G$  ranged from 0.75 to 1.34. When taken together with similar observations from other extraterrestrial samples (Muñoz Caro et al., 2006), these results indicate an intimate mixture of amorphous and nanocrystalline macromolecular matter composed of isolated aromatic domains and disordered sp<sup>2</sup>-bonds. We estimated the aromatic domain size ( $L_a$ ) to range in size from ~1.2 to 1.6 nm<sup>3</sup> or about five benzene (C<sub>6</sub>H<sub>6</sub>) rings (Ferrari and Robertson, 2004), suggesting a close similarity to meteoritic kerogen which accounts for the majority (>90%) of the organic matter in carbonaceous and ordinary chondrites (Sephton and Gilmour, 2000).

A 100 nm thick TEM thin-section (~20 × 20 µm<sup>2</sup>) was extracted from the center of ROI #1 using FIB microscopy (Fig. 3a). In cross-section, the carbonaceous phase appears as a contiguous layer ~5 µm in length and with a thickness ranging from ~50 to 450 nm (Figs. 3b–d and 4a and b). High resolution imaging and selected area electron diffraction show the carbonaceous layer to be amorphous; it lacked long or short range order (*i.e.*, the absence of

<sup>3</sup> Since the intensity of the D band, relative to that of the G band depends strongly on the scattering geometry, the domain sizes estimated from  $I_D/I_G$  ratios are only a rough approximation.



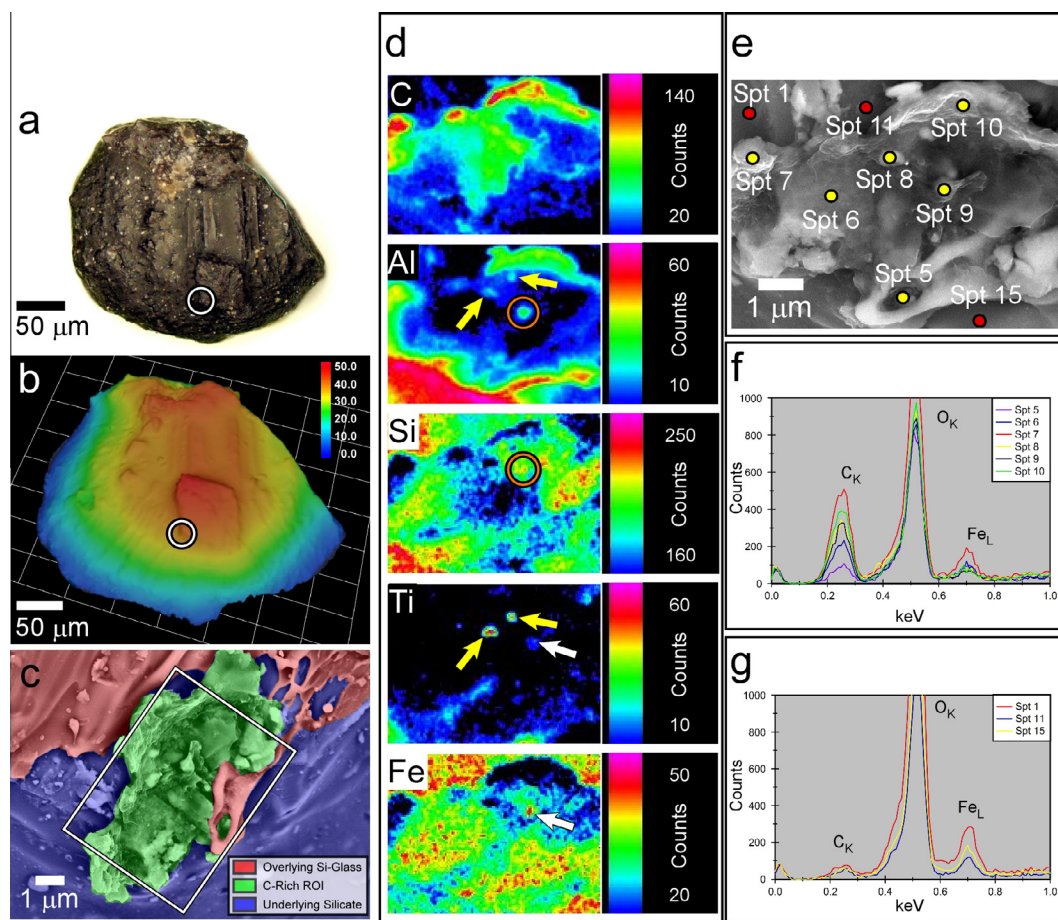


Fig. 1. Optical image, height map, and SEM-EDX data of the C-rich ROI on lunar bead #1. (a) An extended depth-of-field optical image of black glass bead #1 with the position of the C-rich ROI given by the white circle. (b) Associated height-field map of bead #1 showing the C-rich ROI (white circle) is located at the edge of an elevated rhombohedra-shaped plateau on the bead surface. (c) Colorized BSE image of the C-rich ROI (green), partially overlain with glass filament (red) lying on the edge of the plateau (blue). The white box indicates the area for which the EDX element maps shown in d were obtained. (d) EDX element maps for C, Al, Si, Ti and Fe. The two yellow arrows indicate correlated Ti and Al hot-spots consistent with TiO<sub>2</sub> grains, while the white arrows indicate a correlated Ti and Fe hot-spot consistent with an ilmenite grain. The orange circles shows a Si/Al glass inclusion. (e) Expanded BSE image from c showing locations (red/yellow circles) at which 10 kV EDX point spectra were acquired. Yellow circles are on the C-rich ROI while red circles are on the underlying surface. (f) EDX point spectra of C-rich ROI showing counts at the C K<sub>α</sub> line ranging from ~100 to 550 counts channel<sup>-1</sup> (Spt 5–10). Note the lower counts associated with Spt 5 are due to partial obscuration by an overlying glass filament. (g) Comparison EDX point spectra of the underlying surface with counts at the C K<sub>α</sub> line of ≤75 counts channel<sup>-1</sup>.

0.34 nm (002) lattice spacing) that would be characteristic of micro- or nanocrystalline graphite. TEM-EDX spectra and mapping showed that the carbonaceous layer contained O, Mg, Si, and Ca with minor amounts of Na, S, Cl, K, Ti and Fe (Figs. 3e–g and 4c and d). Curiously, element distribution maps of C and Ca correlate with one another. Based on interpretation of TEM and Raman data the Ca-phase is inconsistent with calcite (CaCO<sub>3</sub>), amorphous calcium carbonate, or calcium oxide (CaO). This suggests instead the Ca is ionically bound to the organic phase as a salt. Other element distribution maps show the chemically complex, heterogeneous nature of the C-rich ROI. The presence of Mg, Si, Al and Ti within the C-rich ROI indicate glassy material is intimately embedded with the carbonaceous material. TEM imaging also revealed

the presence of submicron mineral grains, typically <50 nm in size, dispersed within the carbonaceous layer (Figs. 3c–e and 4b). Isolated hotspots of Ti, with associated minor Al, are indicative of a Ti-oxide phase such as rutile. In one case, we identified a Fe–Ni crystallite that, lacking any detectable S, was not a sulfide (Fig. 3g). Underlying the carbonaceous layer is a thin amorphous glassy rim (Figs. 3g and 4d), ~25–100 nm thick. This rim overlies a mixture of olivine ((Mg,Fe)<sub>2</sub>SiO<sub>4</sub>) crystals up to several microns across (Figs. 3b and 4a) intermittently mixed with a finer matrix of glass and olivine nanocrystallites ~200 nm in size (Figs. 3b, e, f and 4a–c). Below this is glass with embedded dendritic FeTiO<sub>3</sub> crystals (Figs. 3b and 4a).

The FIB section containing ROI #1 was subjected to C and N isotopic imaging using a NanoSIMS ion microprobe

Table 1

Results of  $\mu$ -Raman spectroscopy of carbonaceous matter associated with pyroclastic lunar glass beads from sample 74220,861. Aromatic domain size is given by  $L_a$ .

Sample type/name	D peak center (cm <sup>-1</sup> )	G peak center (cm <sup>-1</sup> )	D peak FWHM (cm <sup>-1</sup> )	G peak FWHM (cm <sup>-1</sup> )	$I_D/I_G$	$L_a^*$ (nm)
74220, 861						
<i>Bead #1</i>						
A	1378	1586	320	120	0.97	1.33
B	1371	1590	292	117	0.89	1.27
C	1369	1578	318	129	1.34	1.56
D	1381	1586	317	119	0.99	1.34
E	1371	1597	260	123	0.75	1.17
<i>Bead #2</i>						
6	1358	1588	271	136	1.26	1.52
6A	1361	1586	274	136	1.25	1.50
6E	1374	1585	315	122	1.18	1.46
<i>Bead #3</i>						
C1	1357	1597	205	145	0.77	1.18
C2	1360	1590	270	133	1.25	1.51
Mean $\pm 1\sigma$	1368 $\pm 9$	1588 $\pm 6$	284 $\pm 36$	128 $\pm 9$	1.06 $\pm 0.22$	1.38 $\pm 0.14$

\*  $L_a = 0.1 \times \sqrt{((I_D/I_G)/0.0055)}$  from Muñoz Caro et al. (2006).

(Fig. 5). The carbonaceous rim examined by TEM was found to have  $\delta^{13}\text{C}$  and  $\delta^{15}\text{N}$  values of  $-2.8 \pm 27.9\text{‰}$  and  $-12.8 \pm 19.7\text{‰}$ , respectively. These values are within the respective ranges typical of meteoritic kerogens (Pizzarello et al., 2006). The  $^{12}\text{C}^{14}\text{N}/^{12}\text{C}$  ratio of the carbonaceous rim determined from the NanoSIMS images indicated a bulk N:C ratio in the range of  $\sim 0.1$ – $0.3$ , marginally above the average value of meteoritic kerogen (N:C  $\sim 0.1$  (Pizzarello et al., 2006)).

On glass bead #2 is C-rich ROI #2,  $\sim 3 \times 3 \mu\text{m}^2$ , which overlies a fracture on the surface of the bead (Figs. 6a and b). FESEM-EDX point spectra and subsequent mapping showed within the ROI the C abundance was highly heterogeneous, varying by an order of magnitude at a scale length of less than a micron (Figs. 6c and d). As was observed on ROI #1, mineral grains  $\sim 200$  nm in size were dispersed within the carbonaceous phase. In at least several cases, the presence of Ti enrichments in the embedded grains suggests they are  $\text{TiO}_2$ .  $\mu$ -Raman spectra showed the presence of strong D and G bands and associated second order bands indicating an aromatic carbonaceous material (Table 1 and Figs. 2c and d). The G peak centers ranged from 1585 to 1588  $\text{cm}^{-1}$  with  $G_{\text{FWHM}}$  varying between 122 and 136  $\text{cm}^{-1}$ , and  $I_D/I_G$  ratios ranging from  $\sim 1.18$  to 1.26. This gives a domain size,  $L_a$ , of  $\sim 1.5$  nm, closely matching that for the carbonaceous material on bead #1, again suggesting a similarity to the meteoritic kerogen. Analysis by  $\mu$ - $\text{L}^2\text{MS}$  indicated a concentration of organic species coincident with the ROI, in which mass spectra showed a diverse distribution of peaks ranging up to several hundred atomic mass units (amu), but being most prominent below 100 amu. The presence of low mass peaks at 29, 43, 57 amu, corresponding to simple aliphatic cations ( $\text{CH}_3[\text{CH}_2]_n^+$  where  $n = 1$ – $3$ ), is suggestive of thermally induced fragmentation from a more refractory macromolecular organic precursor such as a kerogen.

The smallest C-rich ROI,  $\sim 2 \times 2 \mu\text{m}^2$  in size, was identified on glass bead #3. The carbonaceous phase is partially obscured by an overlying  $(\text{Mg,Fe})_2\text{SiO}_4$  and/or glass grain (Figs. 7a and b). Consistent with previous FESEM-EDX observations, C was heterogeneously distributed within ROI #3 (Figs. 7c and d) and showed embedded hotspots consistent with submicron mineral grains. Raman spectra show characteristic D and G bands (Table 1 and Figs. 2e and f); the G peak center varied from 1590 to 1597  $\text{cm}^{-1}$ ,  $G_{\text{FWHM}}$  varied between 133 and 145  $\text{cm}^{-1}$ , and  $I_D/I_G$  ranging from 0.77 to 1.25. Again this infers a domain size,  $L_a$ , of  $\sim 1.2$ – $1.5$  nm consistent with the two previous ROIs.

The degree-of-disorder of the carbonaceous matter in the three C-rich ROIs can be qualitatively compared to those of other meteoritic samples through comparison of their Raman spectra; specifically the position of the peak centers and FWHM of the G bands. Based on Raman analysis of IDPs and carbonaceous meteorites in the literature (Ferini et al., 2004; Muñoz Caro et al., 2006; Busemann et al., 2007), all the C-rich ROIs have a degree-of-disorder similar to that of most primitive astromaterials available for study (Fig. 2g).

## 5. DISCUSSION

Several lines of evidence argue against a terrestrial source for the organic matter observed herein. The chain of custody prior to our analyses is well documented and in accordance with lunar curation sample handling protocols (Allton, 1998). All samples were kept in pristine condition until opened in a lunar glove box under dry  $\text{N}_2$  in 2012. Exposure of the samples to the laboratory atmosphere was strictly limited, and when not being analyzed, the samples remain stored under dry  $\text{N}_2$ . One of the three ROIs was partially covered by siliceous matter indicating it was present on bead surfaces prior to being collected. All are

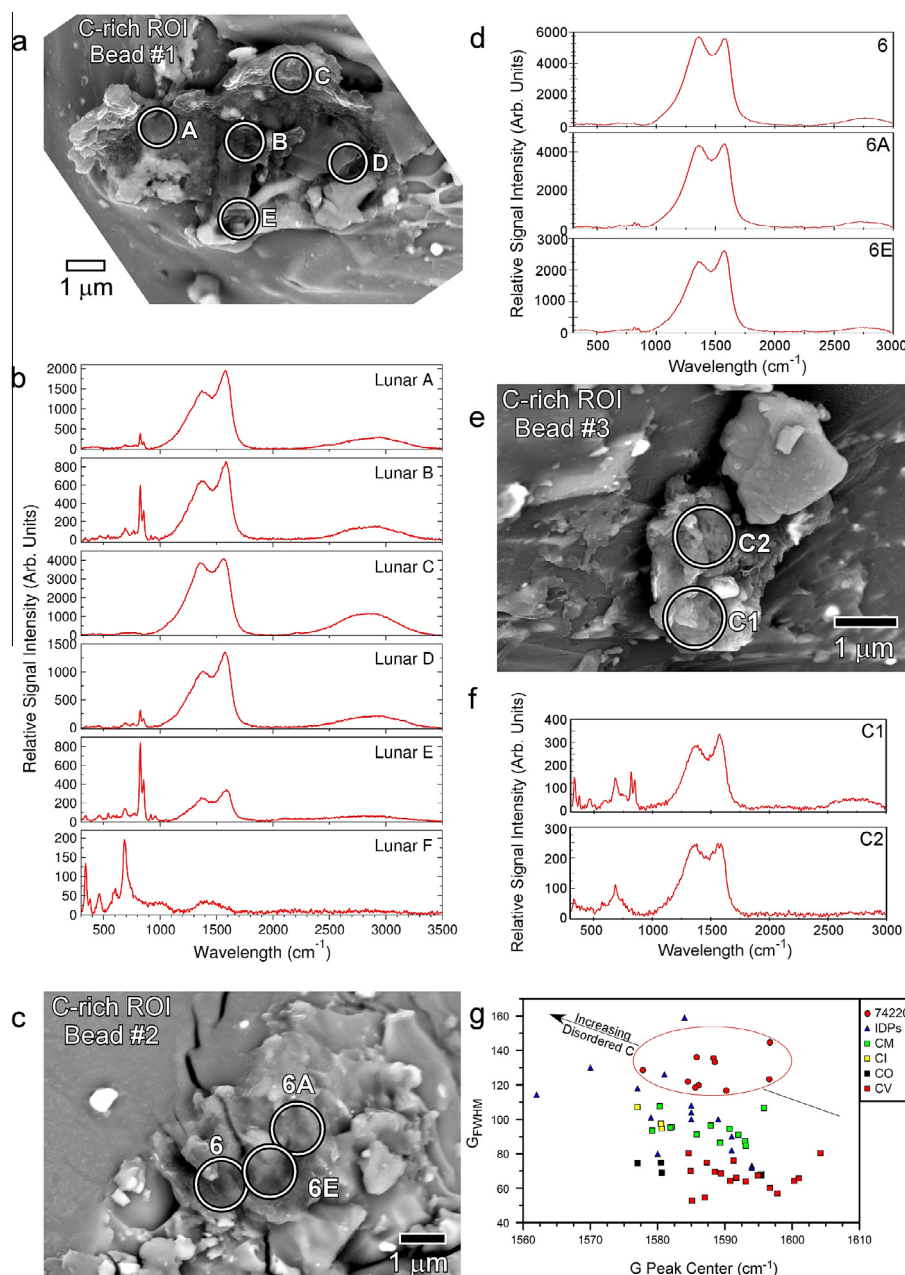


Fig. 2. Raman spectra of the three C-rich ROIs associated with 74220,861 lunar glass beads. (a) BSE image of the C-rich ROI on bead #1 showing locations of Raman analyses. (b) Raman spectra of the C-rich ROI shown in a (Spt A–E) and background (Spt F). First order bands at  $\sim 1350$  and  $1580\text{--}1600\text{ cm}^{-1}$  represent D and G bands, respectively. Peaks located below  $1000\text{ cm}^{-1}$  correspond to olivine (peak doublet at  $\sim 800\text{--}850\text{ cm}^{-1}$ ) and ilmenite ( $\sim 700\text{ cm}^{-1}$ ). Note C-rich matter is detected through the hole in the siliceous filament in spectrum Lunar E. (c) BSE image of the C-rich ROI on bead #2 showing locations of Raman analyses. (d) Raman spectra of the C-rich ROI shown in c. First order bands at  $\sim 1350$  and  $1580\text{--}1600\text{ cm}^{-1}$  represent D and G bands, respectively. (e) BSE image of the C-rich ROI on bead #3 showing locations of Raman analyses. (f) Raman spectra of the C-rich ROI shown in e. First order bands at  $\sim 1350$  and  $1580\text{--}1600\text{ cm}^{-1}$  represent D and G bands, respectively. Peaks located below  $1000\text{ cm}^{-1}$  correspond to olivine (peak doublet at  $\sim 800\text{--}850\text{ cm}^{-1}$ ) and ilmenite ( $\sim 700\text{ cm}^{-1}$ ). (g) Comparison of Raman data for 74220 C-rich ROIs (red ellipse) with IDPs (data from (Ferini et al., 2004; Muñoz Caro et al., 2006)) and CM, CO, CI, CV-type carbonaceous chondrites (data from (Busemann et al., 2007)). Carbonaceous matter predominantly composed of amorphous, structurally disordered C plots near the upper left corner of the graph.

composed primarily of amorphous, structurally disordered kerogen-like organic matter composed of a patchwork macromolecular structure formed by the random combination

of many small molecular fragments dissimilar to terrestrial contamination. The organic material in the ROIs studied was refractory, that is, it did not vesiculate or decompose



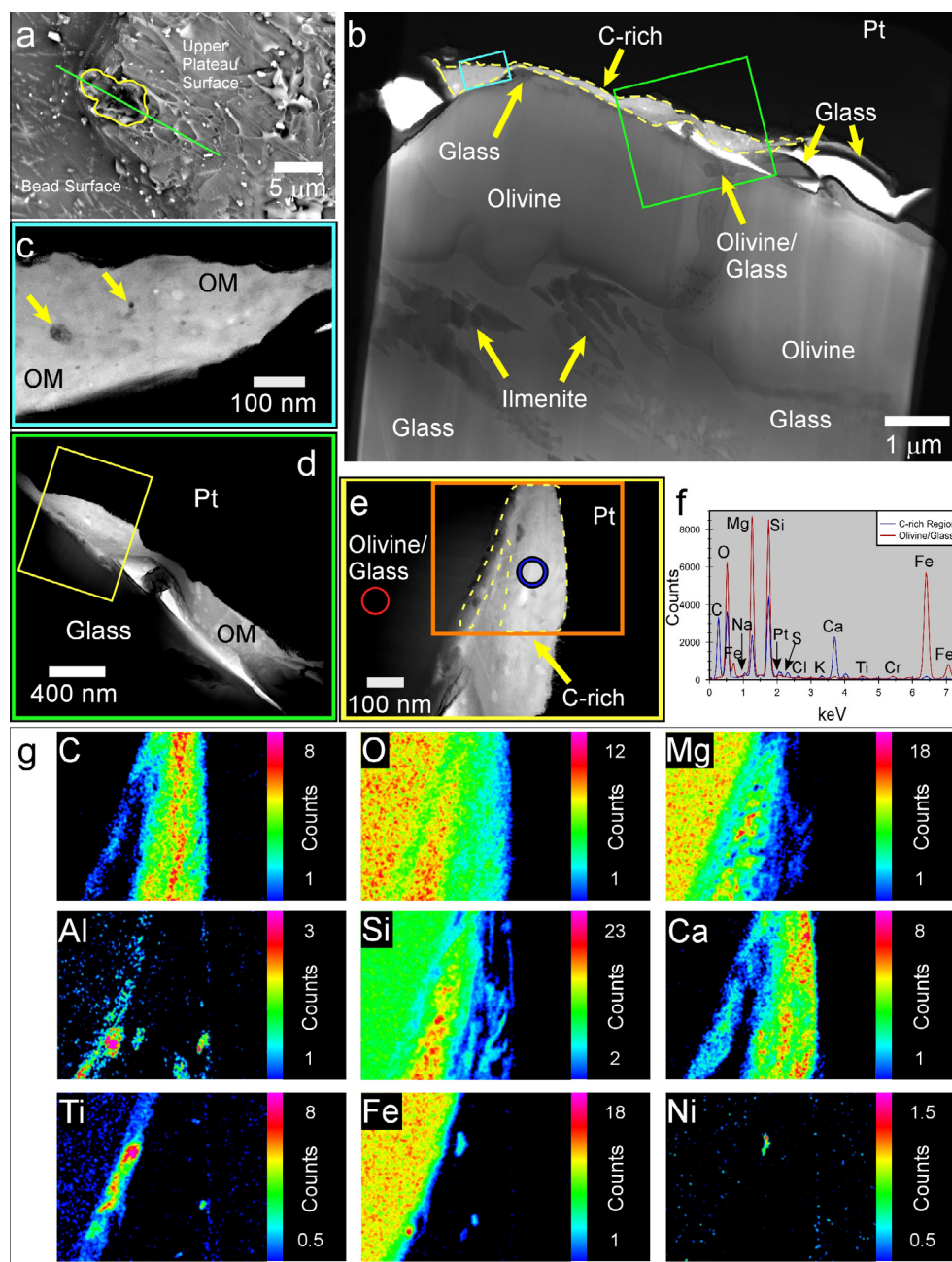


Fig. 3. Location of the FIB-extracted thin section and TEM-EDX data of the thin section extracted from the C-rich ROI on lunar bead #1. (a) BSE image of the C-rich ROI on the black glass bead #1 outlined in yellow and traversed with a green line showing the location from which a thin-section was extracted by FIB microscopy. (b) STEM image of the upper portion of the extracted FIB section with C-rich region outlined by a yellow dashed line. The blue and green boxes show the locations of the expanded views shown in c and d, respectively. (c) Expanded view of FIB section showing the light gray region, composed of organic matter (OM), in which are embedded nanophase (<50 nm) mineral grains as indicated by the yellow arrows. (d) Expanded STEM view of a second region of organic matter, also containing embedded nanophase mineral grains. The yellow box shows the location of the expanded view shown in e. (e) High magnification STEM view of the organic – glass/olivine interface. The red and blue circles mark the positions of the point EDX spectra shown in f, while the orange box shows the region for which individual EDX element maps shown in g were acquired. (f) EDX point spectra of the organic matter and underlying olivine/glass shown in e. The organic phase is composed primarily of C, Mg, Si and Ca with minor Na, S, Cl, K and Fe implying an intimate mixture of organic matter, glass, and an amorphous Ca-bearing phase inconsistent with carbonate. The underlying surface is composed of a Si-rich glass with minor to trace amounts of Ti and Cr intermixed with olivine; (g) EDX element maps from the area indicated by the orange box in e. The correlation of C with O suggests the organic phase is partially oxidized, i.e., has oxygen containing functionalities. The Si/Mg maps show that glass-like bands and/or hotspots are intimately mixed with the organic matter, along with nanophase (<50 nm) crystallites, containing Al (likely glass), Ti (likely  $\text{TiO}_2$ ), Fe (metal), and Fe–Ni (metal).



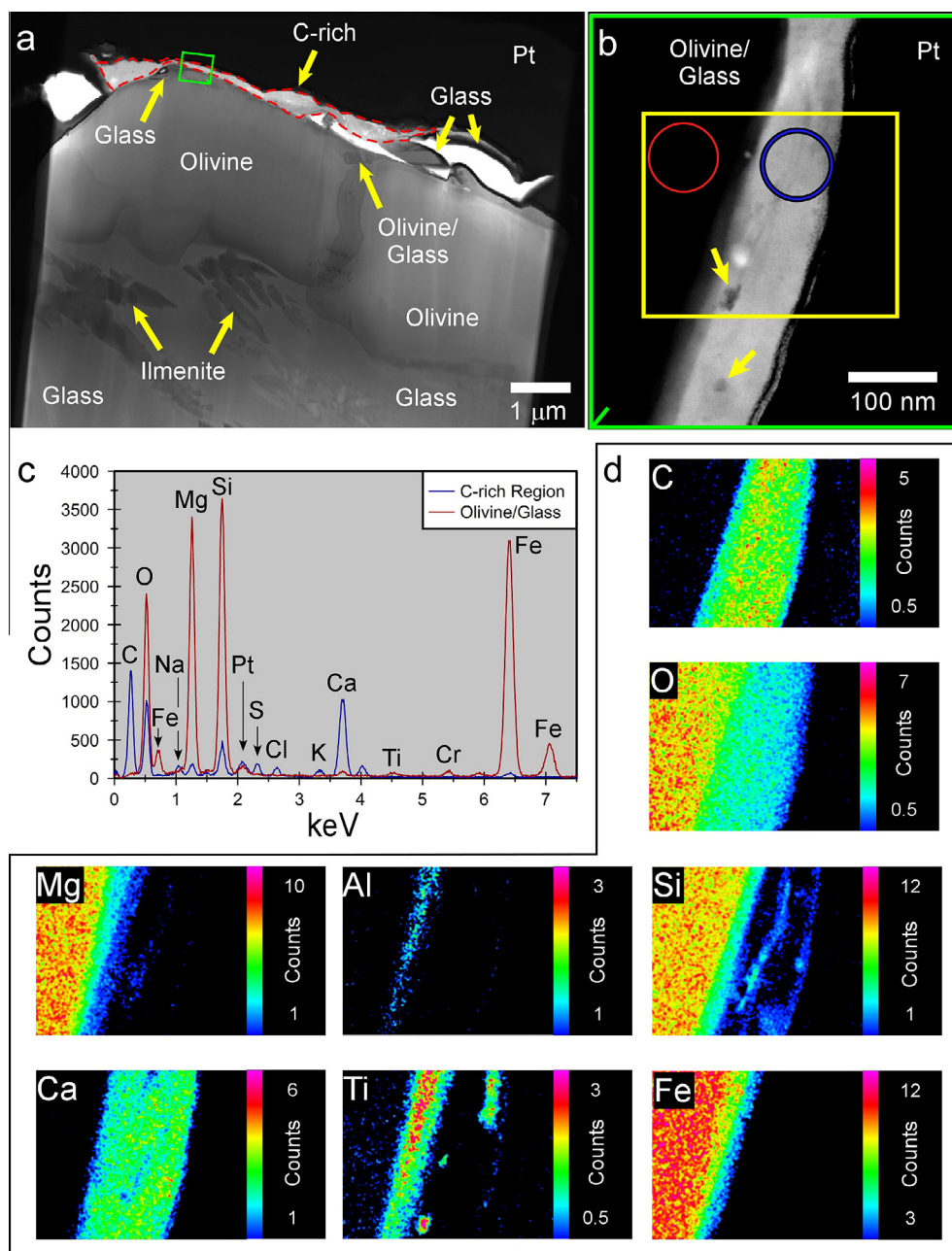


Fig. 4. Analysis of FIB section extracted from sample 74220 bead #1. (a) STEM image with C-rich region outlined by a red dashed line; green box demarcates region shown in b. (b) Expanded view showing carbonaceous matter (light gray region) with embedded nanophase (<50 nm) mineral grains, indicated by yellow arrows. Red and blue circles mark the positions of the point EDX spectra shown in c; the yellow box marks the field over which the EDX element maps in d were acquired. (c) EDX spectra of carbonaceous matter and underlying olivine/glass. The carbonaceous region is composed primarily of C, Ca and O with minor Si and Mg and trace Al, indicating the organic phase intimately mixed with glass and an amorphous non-carbonate Ca-bearing phase. (d) EDX element maps of region shown in b. Correlation of C with O suggests the organic phase is at least partially oxidized. The Si map shows that glass-like bands and/or hotspots are intimately mixed with the organic matter, along with nanophase (<100 nm) crystallites containing Ti (likely  $\text{TiO}_2$  or a  $\text{TiO}_2$  precursor phase).

during analysis when subjected to vacuum exposure and laser/electron beam irradiation. This is consistent with prior survival in the vacuum and radiation environment of the lunar regolith. As such, this material is comparable to the insoluble macromolecular material present within carbonaceous chondrites (Sephron, 2005). Additionally, embedded

within the kerogen matrix are discrete crystallites <50 nm in size composed of  $\text{TiO}_2$ ,  $\text{Fe}^0$ , and Fe–Ni metal, and bands and/or hotspots of Si-rich glass, phases commonly associated with lunar materials.

Presence of organic matter in the lunar environment could be envisioned to have occurred through several

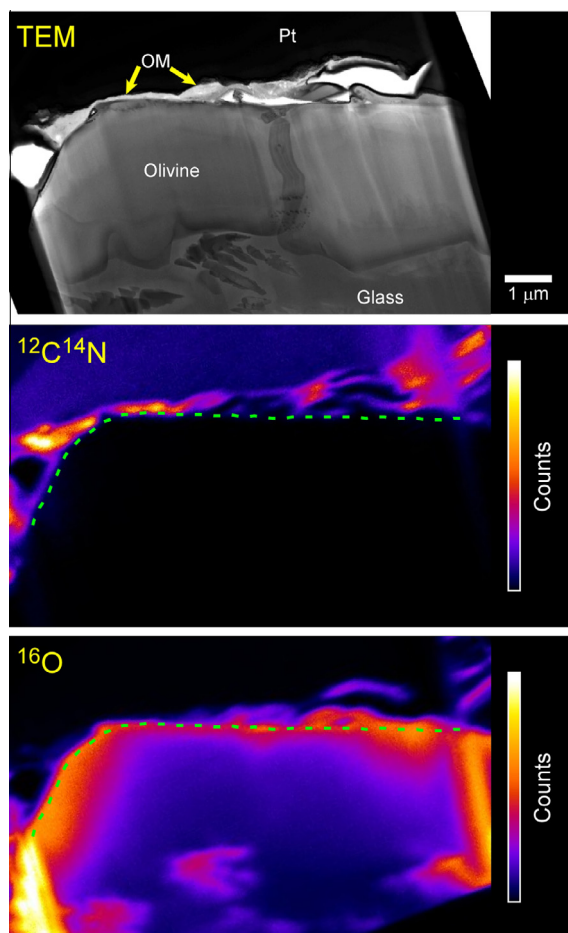


Fig. 5. STEM view and NanoSIMS isotope maps of the FIB section extracted from the C-rich ROI on bead #1. STEM image (top) and corresponding NanoSIMS isotope maps, for  $^{12}\text{C}^{14}\text{N}$  (middle) and  $^{16}\text{O}$  (bottom), for the FIB section extracted from lunar sample 74220 bead #1. The overlaid green dashed line in the isotope maps marks the upper olivine surface of the bead. Organic matter (OM) which appears as the thin grey region overlying the olivine surface in the STEM image is enriched in both N and O.

scenarios. The first is through the interaction of the solar wind and solar radiation with the lunar regolith. The 74220 glass beads spent at least some time at the regolith surface, where exposure to the solar wind leads to surficial implantation of H, C and N (Warren and Haskin, 1991). These implanted elements can subsequently react to form simple hydrocarbons such as  $\text{CH}_4$  and its deuterated counterpart ( $\text{CD}_4$ ) (Pillinger et al., 1972). More complex hydrocarbons may also subsequently form through photolysis and radical recombination reactions. Given the nature of the C-ROIs and the limited exposure histories ( $\sim 20$  Ma) of the glass beads, it is difficult to envision the contribution from this process being significant enough as to result in the formation of micrometer size C-rich hotspots.

In the second scenario, hydrocarbons could have been produced in outgassing during the fire-fountaining events that produced the glass beads. The observation of  $\text{H}_2\text{O}$  trapped within olivine melt inclusions within 74220 volcanic

glass beads (Hauri et al., 2011) implies that the magma source was  $\text{H}_2\text{O}$ -bearing, while the driving force for the fire fountaining events are thought to have been due to the explosive oxidation of graphite in the pre-ejection magma to carbon monoxide (CO) and  $\text{CO}_2$ . The interaction of CO/ $\text{CO}_2$  with  $\text{H}_2\text{O}$  vapor in the hot turbulent environment of the ejection plume could have led to the synthesis of various simple hydrocarbons via the Boudouard reaction ( $2\text{CO} \rightleftharpoons \text{CO}_2 + \text{C}$ ), the Water–Gas Shift reaction ( $\text{CO} + \text{H}_2\text{O} \rightarrow \text{CO}_2 + \text{H}_2$ ), and the Fischer–Tropsch–Type reactions ( $((2n+1)\text{H}_2 + n\text{CO}_2 \rightarrow \text{C}_n\text{H}_{2n+2} + n\text{H}_2\text{O})$ ; the latter being heterogeneously catalyzed by the surfaces of glass beads. Nevertheless it is unclear how simple hydrocarbons could be subsequently transformed into the localized concentrations of macromolecular material observed and so we consider contributions via this route also to have been insignificant.

The third scenario involves the exogenous addition of organic matter derived from the accretion of asteroidal and cometary sources. Analyses of stratospherically collected IDPs and Antarctic micrometeorites indicates the micrometeorite flux is dominated by fine-grained aggregates with compositions similar to CI and CM meteorites but with significantly higher C abundances (Thomas et al., 1993) present primarily as organic matter (Clemett et al., 1993). On Earth, it has been speculated that exogenous accretion may have contributed significantly to the planet's prebiotic organic inventory (Flynn et al., 2004), and on the Moon, it is known fragments of carbonaceous meteorites survive accretion (Zolensky, 1997). The contribution of organic matter to the lunar surface by exogenous sources can be estimated from measurements of the terrestrial micrometeorite flux. Based on examination of hypervelocity impact craters on the space-facing end of the Long Duration Exposure Facility satellite (Love and Brownlee, 1993), the terrestrial accretion rate for meteoroids in the mass range  $10^{-9}$  to  $10^{-4}$  g is  $(40 \pm 20) \times 10^6 \text{ kg year}^{-1}$  with a mass distribution that peaks near  $1.5 \times 10^{-5}$  g. The lunar flux  $F_{\text{Moon}}$  can be related to the terrestrial flux  $F_{\text{Earth}}$  by the gravitational focusing factor  $k$  (Vanzani et al., 1997), where:

$$F_{\text{Moon}} = k \cdot F_{\text{Earth}} = \left[ \frac{v_{\text{Moon}}}{v_{\text{Earth}}} \right]^2 \cdot F_{\text{Earth}}$$

Where  $v_{\text{Moon}}$  and  $v_{\text{Earth}}$  are the average entry velocities for the Moon and the Earth and have values of  $\sim 13.3$  and  $16.9 \text{ km s}^{-1}$  (Vanzani et al., 1997) so that  $k \sim 0.62$ . From this we can estimate the annual mass of exogenously accreted matter,  $\int_0^1 F_{\text{Moon}} \cdot dt$ , on the Moon to be  $\sim 1.21 \times 10^6 \text{ kg year}^{-1}$ . To determine the mass fraction of the lunar regolith represented by this exogenous material we need to know the age and depth of the regolith. Using the relationship between the near-surface exposure ages of lunar soil and the reworking depths in the regolith as measured in Apollo 15, 16 and 17 samples (McKay et al., 1991), we estimate that the first 10 cm of the lunar regolith has an average exposure age,  $\tau$ , of  $\sim 10^8$  years. If  $R_{\text{Moon}}$  is the radius of the Moon and  $\rho_{\text{regolith}}$  is the mean density of regolith then the mass of the first 10 cm of regolith is,  $M_{\text{regolith}}$ , given by:

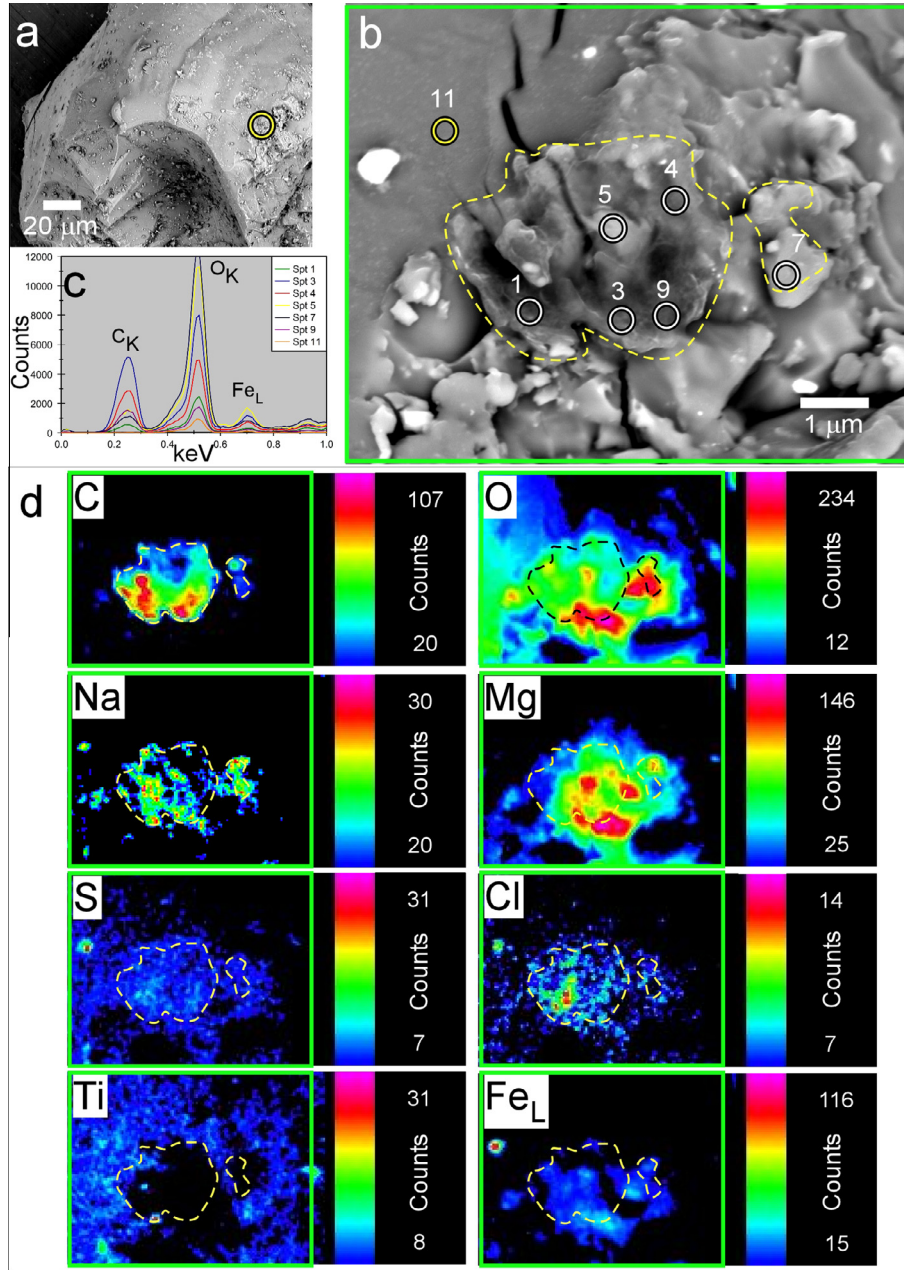


Fig. 6. SEM images and corresponding EDX data from the C-rich ROI on lunar bead #2. (a) BSE view of the surface of lunar sample 74220 black glass bead #2 showing the location of the C-rich ROI (yellow circle). (b) BSE view of the C-rich ROI outlined by the dashed yellow line. Circles (white/yellow) show locations of EDX point spectra. The green box indicates the area for which the EDX element maps shown in d were obtained. (c) EDX point spectra of C-rich ROI showing counts at the C  $K_{\alpha}$  line ranging from ~700 to 5500 counts channel<sup>-1</sup>. Comparison EDX point spectrum of the underlying surface (Spt 11) with counts at the C  $K_{\alpha}$  line of  $\leq 50$  counts channel<sup>-1</sup>. (d) EDX element maps for C, O, Na, Mg, S, Cl, Ti and Fe. Dashed outlines in each map correspond to the C-rich ROI.

$$M_{\text{regolith}} = \frac{4}{3} \cdot \pi \cdot \rho_{\text{regolith}} \cdot (R_{\text{Moon}}^3 - [R_{\text{Moon}} - 0.1]^3)$$

Using  $R_{\text{Moon}} = 1.7371 \times 10^6$  m and  $\rho_{\text{regolith}} \sim 2450$  kg m<sup>3</sup> this gives  $M_{\text{regolith}} \sim 9.3 \times 10^{15}$  kg. Assuming the exogenous contribution to  $M_{\text{regolith}}$  is small enough that we can ignore its effect on the estimated exposure age, the mass of material derived from exogenous accretion is simply given by:

$$M_{\text{accreted}} = \tau \cdot \int_0^{1 \text{ yr}} F_{\text{Moon}} \cdot dt$$

For which  $M_{\text{accreted}} \sim 1.21 \times 10^{14}$  kg, and so the mass fraction of exogenous material in the top 10 cm of the lunar regolith is simply:

$$\frac{M_{\text{accreted}}}{M_{\text{regolith}}} \simeq 0.013$$



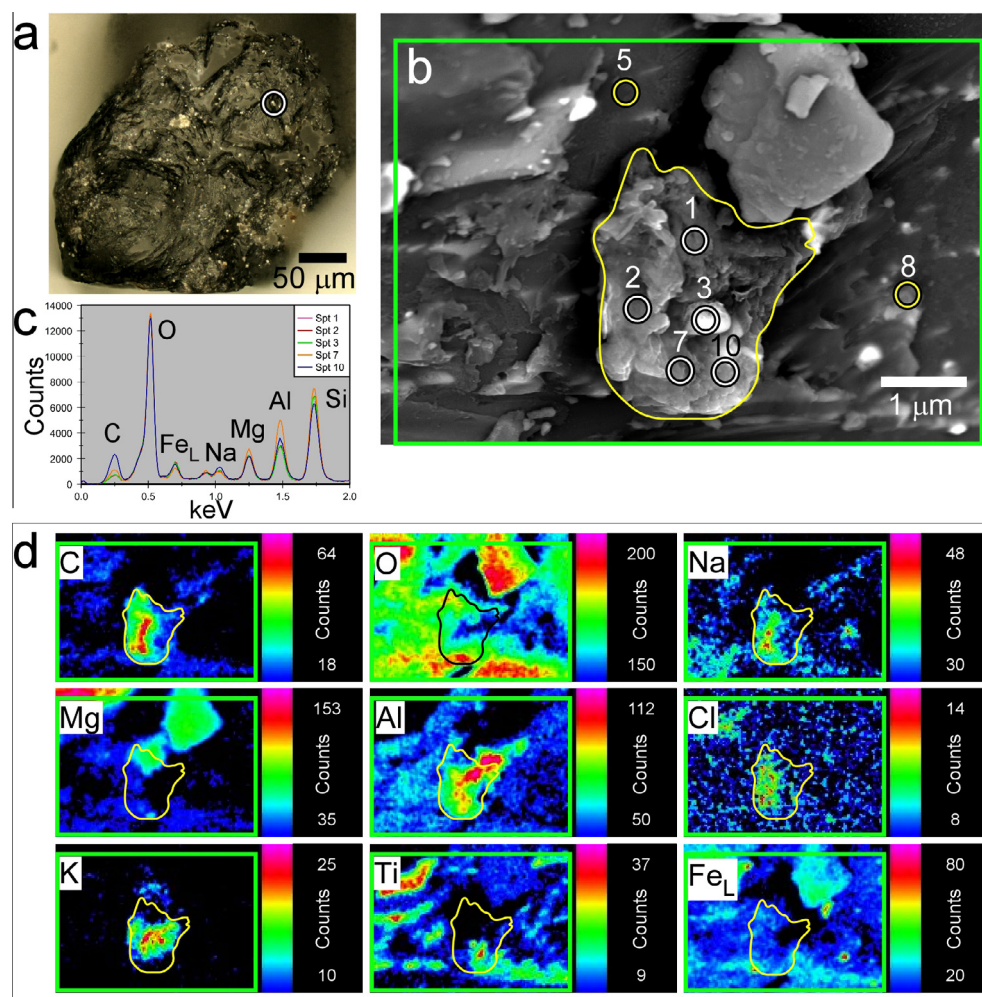


Fig. 7. Optical, SEM images and corresponding EDX data from the C-rich ROI on lunar bead #3. (a) An extended depth-of-field optical image of lunar sample 74220 black glass bead #3 with the position of the C-rich ROI given by the white circle. (b) BSE image of the C-rich ROI, outlined in yellow, showing locations (white/yellow circles) at which 10 kV EDX point spectra were acquired. The green box indicates the area for which the EDX element maps shown in d were obtained. (c) EDX point spectra of C-rich ROI showing counts at the C  $K_{\alpha}$  line ranging from  $\sim 750$  to  $2500$  counts  $\text{channel}^{-1}$ . Comparison EDX point spectrum of the underlying surface (Spt 5, 8) with counts at the C  $K_{\alpha}$  line of  $\leq 500$  counts  $\text{channel}^{-1}$  (not shown). (d) EDX element maps for C, O, Na, Mg, Al, Cl, K, Ti and Fe. Outlines in each map correspond to the C-rich ROI. Hotspots for Ti likely correspond to  $\text{TiO}_2$ .

That is, to first order, we can expect  $\sim 1.3\%$  by mass of the surface regolith to be exogenously acquired. If this exogenous material has chondritic element abundances (*i.e.*,  $\sim 35,180 \mu\text{g C g}^{-1}$  (Pearson et al., 2006)), then the C contribution from exogenous sources is on the order of  $460 \mu\text{g g}^{-1}$  (ppm). Interestingly this is  $\sim 4\times$  greater than the maximum reported (Fegley and Swindle, 1993). This is likely a lower limit since the flux is not constant and would have been considerably higher (Whittet, 1997) shortly after the period of late heavy bombardment (4.1–3.8 Ga) when the volcanic glass beads formed.

Given the expected lunar accretion rates and the abundance of meteoritic organics we suggest the most probable source of the observed organic matter is from the exogenous addition of asteroidal and cometary matter. Since we found no clear evidence for any associated inorganic meteoritic phases in the three carbonaceous ROIs studied we suggest formation occurred by the redeposition of

impact volatilized meteoritic organics. Since such a process would be ostensibly under kinetic as opposed to thermodynamic control, the recondensed organic phase would be characterized by a high degree of disorder as observed in the individual Raman spectra (Fig. 2).

## 6. CONCLUSIONS

The C-rich ROIs identified on the surfaces of the 74220 pyroclastic beads represent the first identification of complex organic matter associated with any lunar sample. Previous reports of C in lunar samples have been restricted to only inorganic phases including: graphite in Apollo 17 impact melt breccia 72255 (Steele et al., 2010); graphite, nanographite, nanodiamonds (Dikov et al., 1998) and Zn–C films (Dikov et al., 2002b) in Luna 16 soil sample 1635; and, silicon carbide (SiC) and graphite in 74220 orange glass beads (Dikov et al., 2002a).



Our work has revealed that non-terrestrial, complex organic matter is intimately associated with Apollo 17 lunar glass beads. Organic molecules were contributed by asteroidal fragments and cometary matter to the surfaces of the early Moon and Earth. Implicit in the proposed model is that at least some fraction of the organic component of micrometeorites and IDPs survived impact into the lunar regolith. The lunar micrometeoroid velocity distribution is bound on the lower side by the Moon's escape velocity ( $2.4 \text{ km s}^{-1}$ ) and on the upper side by the sum of the Earth's orbital velocity at 1 A.U. and the escape velocity of the Solar System ( $72 \text{ km s}^{-1}$ ), with a modal velocity of  $13\text{--}18 \text{ km s}^{-1}$  (Zook, 1975). While even at the lowest entry velocities a significant fraction of micrometeorites will be vaporized, experimental and observational evidence supports survival of at least some carbonaceous matter. Laboratory studies of organic matter in hypervelocity impacts, analogous to impacts onto planetary surfaces, found partial survival even at shock pressures as high as 30 GPa (Cooper et al., 2013). Observational evidence includes the near-infrared reflectance (NIR) spectra of simple  $\text{C}_1\text{--C}_2$  organics in the ejecta plume produced by the impact of the Lunar CRater Observation and Sensing Satellite (LCROSS) into a persistently shadowed region of the south polar crater Cabeus (Colaprete et al., 2010). Similarly, NIR surface reflectance measurements of permanently shadowed areas of craters near Mercury's north pole revealed regions of anomalously dark material consistent with a surface layer of complex organic material (Neumann et al., 2012). From the preceding discussion and given the noted similarities between the carbonaceous matter present on 74220 glass beads and meteoritic kerogen, we suggest the exogenous addition of meteoritic organics as the most probable source for the C-ROIs.

The main implication of this study is that we need to reevaluate the prevailing perception of the Moon as a body devoid of organic matter. Meteoritic accretion has likely played a profound role in shaping the evolution of the lunar regolith. Additionally continued investigations of such organic matter, uncontaminated and unmodified by the terrestrial environment, will provide new perspectives in understanding the prebiotic chemical inventory of the early Earth.

#### ACKNOWLEDGEMENTS

Funding was provided by the NASA Cosmochemistry program, grant 11 COS11-0049. We thank L. Watts and J. Allton for their contribution to the history of Apollo sample 74220. We express our sincere gratitude to Dr. Scott Kopetz and Dr. George Chang and their staffs for their support. We also thank S. Keperta, N. Keperta, M. Walheim, S. Wentworth, O. Clemett and C. Clemett for their continued encouragement. We thank the reviewers for comments that improved the quality of the manuscript. We gratefully acknowledge the guidance and friendship of world-renowned lunar scientist, Dr. David McKay, who passed away on February 19, 2013.

#### REFERENCES

Alexander E. C. J., Coscio M. R. J., Dragon J. C. and Saito K. (1980) K/Ar dating of lunar soils. IV – orange glass from 74220

- and agglutinates from 14259 and 14163. *Proc. Lunar Planet. Sci. Conf.* **XI**, 1663–1677.
- Allton J. H. (1998) A brief history of organic contamination monitoring of lunar sample handling. *Lunar Planet. Sci. Conf.* **XXIX**, #1857.
- Anders E. (1989) Pre-biotic organic matter from comets and asteroids. *Nature* **342**, 255.
- Arndt J. and Engelhardt W. V. (1986) Cooling history of Apollo 17 orange and black glasses: implications for their formation. *Lunar Planet. Sci. Conf.* **XVII**, 15–16.
- Beyssac O., Goffé B., Chopin C. and Rouzaud J. N. (2002) Raman spectra of carbonaceous material in metasediments: a new geothermometer. *J. Metamorph. Geol.* **20**, 859–871.
- Blanchard D. P. and Budahn J. R. (1978) Compositional variations among size fractions in a homogeneous, unmatured regolith: drive tube 74001/2. *Lunar Planet. Sci. Conf.* **IX**, 100–102.
- Bogard D. D. and Hirsch W. C. (1978) Depositional and irradiational history and noble gas contents of orange-black droplets in the 74002/1 core from Shorty Crater. *Proc. Lunar Planet. Sci. Conf.* **IX**, 1981–2000.
- Burlingame A. L., Calvin M., Han J., Henderson W., Reed W. and Simoneit B. R. (1970) Lunar organic compounds: search and characterization. *Science* **167**, 751–752.
- Busemann H., O'D Alexander C. and Nittler L. (2007) Characterization of insoluble organic matter in primitive meteorites by microRaman spectroscopy. *Meteorit. Planet. Sci.* **42**, 1387–1416.
- Chyba C. and Sagan C. (1992) Endogenous production, exogenous delivery and impact-shock synthesis of organic molecules: an inventory for the origins of life. *Nature* **355**, 125–132.
- Clemett S. J., Maechling C. R., Zare R. N., Swan P. D. and Walker R. M. (1993) Identification of complex aromatic molecules in individual interplanetary dust particles. *Science* **262**, 721–725.
- Colaprete A., Schultz P., Heldmann J., Wooden D., Shirley M., Ennico K., Hermalyn B., Marshall W., Ricco A., Elphic R. C., Goldstein D., Summy D., Bart G. D., Asphaug E., Korycansky D., Landis D. and Sollitt L. (2010) Detection of water in the LCROSS ejecta plume. *Science* **330**, 463–468.
- Cooper G., Horz F., O'leary A. and Chang S. (2013) The impact and oxidation survival of selected meteoritic compounds: signatures of asteroid organic material on planetary surfaces. *Lunar Planet. Sci. Conf.* **XLIV**, #1868.
- Crozaz G. (1979) Regolith reworking at Shorty Crater. *Proc. Lunar Planet. Sci. Conf.* **X**, 1381–1384.
- Dikov Y. P., Ivanov A. V., Wlotzka F., Galimov E. M. and Wanke H. (1998) High enrichment of carbon and volatile elements in the surface layers of Luna 16 soil sample 1635. *Earth Planet. Sci. Lett.* **155**, 197–204.
- Dikov Y. P., Gorshkov A. I., Sivtsov A. I., Wlotzka F. and Ivanov A. V. (2002) SiC and graphite in the sublimate layer of lunar orange glass spherules. *Lunar Planet. Sci. Conf.* **XXXIII**, #1186.
- Dikov Y. P., Ivanov A. V., Wlotzka F., Galimov E. M. and Wanke G. (2002) The nature of volatiles in the lunar regolith. *Sol. Syst. Res.* **36**, 1–11.
- Escudero A., Delevoye L. and Langenhorst F. (2011) Aluminum incorporation in  $\text{TiO}_2$  at high pressure: an XRD and high-resolution  $^{27}\text{Al}$  NMR study. *J. Phys. Chem.* **115**, 12196–12201.
- Eugster O., Eberhardt P., Geiss J., Groegler N., Jungck M. and Moergeli M. (1977) The cosmic-ray exposure history of Shorty Crater samples – the age of Shorty Crater. *Proc. Lunar Sci. Conf.* **VIII**, 3059–3082.
- Fegley B. J. and Swindle T. D. (1993) Lunar volatiles: implications for lunar resource utilization. In *Resources of Near-Earth Space* (eds. J. S. Lewis, M. Shapley Matthews and M. L. Guerrieri). University of Arizona Press, Tucson, pp. 367–426.

- Ferini G., Baratta G. A. and Palumbo M. E. (2004) A Raman study of ion irradiated icy mixtures. *Astron. Astrophys.* **414**, 757–766.
- Ferrari A. C. (2007) Raman spectroscopy of graphene and graphite: disorder, electron-phonon coupling, doping and nonadiabatic effects. *Solid State Commun.* **143**, 47–57.
- Ferrari A. C. and Robertson J. (2000) Interpretation of Raman spectra of disordered and amorphous carbon. *Phys. Rev. B* **61**, 14095–14107.
- Ferrari A. C. and Robertson J. (2004) Raman spectroscopy of amorphous, nanostructured, diamond-like carbon, and nanodiamond. *Philos. Trans. R. Soc. A* **362**, 2477–2512.
- Fleischer R. L., Hart H. R. and Giard W. R. (1974) Surface history of lunar soil and soil columns. *Geochim. Cosmochim. Acta* **38**, 365–380.
- Flynn G., Keller L. P., Jacobsen C., Wirick S., Miller M. A. and Meech K. (2000). Organic carbon in interplanetary dust particles. In: *Bioastronomy 99: A New Era in the Search for Life* (eds. G. Lemarchand, K. Meech). pp. 191–194.
- Flynn G. J., Keller L. P., Jacobsen C. and Wirick S. (2004) An assessment of the amount and types of organic matter contributed to the Earth by interplanetary dust. *Adv. Space Res.* **33**, 57–66.
- Forster B., Van De Ville D., Berent J., Sage D. and Unser M. (2004) Complex wavelets for extended depth-of-field: a new method for the fusion of multichannel microscopy images. *Microsc. Res. Tech.* **65**, 33–43.
- Gehrke C. W., Zumwalt R. W., Kuo K. C., Ponnampuruma C., Cheng C.-N. and Shimoyama A. (1973) Extractable organic compounds in Apollo 15 and 16 lunar fines. *Proc. Fourth Lunar Planet. Sci. Conf.*, 2249–2259.
- Gilvarry J. J. (1960) Origin and nature of lunar surface features. *Nature* **188**, 886–891.
- Hauri E. H., Weinreich T., Saal A. E., Rutherford M. C. and Van Orman J. A. (2011) High pre-eruptive water contents preserved in lunar melt inclusions. *Science* **333**, 213–215.
- Heiken G. and McKay D. S. (1977) A model for eruption behavior of a volcanic vent in eastern Mare Serenitatis. *Proc. Lunar Sci. Conf. VIII*, 3243–3255.
- Heiken G. H., McKay D. S. and Brown R. W. (1974) Lunar deposits of possible pyroclastic origin. *Geochim. Cosmochim. Acta* **38**, 1703–1718.
- Hlava P. F., Prinz M. and Keil K. (1972) Niobian Rutile in an Apollo 14 KREEP Fragment. *Meteoritics* **7**, 479–485.
- Huneke J. C. (1978) Ar-40-Ar-39 microanalysis of single 74220 glass balls and 72435 breccia clasts. *Proc. Lunar Planet. Sci. Conf. IX*, 2345–2362.
- King B. V., Pellin M. J., Moore I. V., Veryovkin I. V., Savina M. R. and Tripa C. E. (2003) Estimation of useful yield in surface analysis using single photon ionization. *Appl. Surf. Sci.* **203**(204), 244–247.
- Kirsten T., Horn P. and Heymann D. (1973) Chronology of the Taurus-Littrow region I: ages of two major rock types from the Apollo 17-site. *Earth Planet. Sci. Lett.* **20**, 125–130.
- Knight D. S. and White W. B. (1989) Characterization of diamond films by Raman spectroscopy. *J. Mater. Res.* **4**, 385–393.
- Lockyer N. P. and Vickerman J. C. (1997) Single photon ionization mass spectrometry using laser-generated vacuum ultraviolet photons. *Laser Chem.* **17**, 139–159.
- Love S. G. and Brownlee D. E. (1993) A direct measurement of the terrestrial mass accretion rate of cosmic dust. *Science* **262**, 550–553.
- McKay D. S., Heiken G., Basu A., Blanford G., Simon S., Reedy R. C., French B. M. and Papike J. (1991). In *The Lunar Regolith* (eds. D. T. Vaniman and B. M. French). Cambridge University Press, New York, pp. 284–356.
- Meyer, Jr., C., McKay D. S., Anderson D. H. and Butler, Jr., P. (1975) The source of sublimates on the Apollo 15 green and Apollo 17 orange glass samples. *Proc. Lunar Planet. Sci. Conf. VI*, 1673–1699.
- Muñoz Caro G. M., Matrajt G., Dartois E., Nuevo M., D'Hendecourt L., Deboffe D., Montagnac G., Chauvin N., Boukari C. and Le Du D. (2006) Nature and evolution of the dominant carbonaceous matter in interplanetary dust particles: Effects of irradiation and identification with a type of amorphous carbon. *Astron. Astrophys.* **459**, 147–159.
- Neumann G. A., Cavanaugh J. F., Sun X., Mazarico E. M., Smith D. E., Zuber M. T., Mao D., Paige D. A., Solomon S. C., Ernst C. M. and Barnouin O. S. (2012) Bright and dark polar deposits on mercury: evidence for surface volatiles. *Science* **339**, 296–300.
- Pearson V. K., Sephton M. A., Franchi I. A., Gibson J. M. and Gilmour I. (2006) Carbon and nitrogen in carbonaceous chondrites: elemental abundances and stable isotopic compositions. *Meteorit. Planet. Sci.* **41**, 1899–1918.
- Pillinger C. T., Cadogan P. H., Eglinton G., Maxwell J. R., Mays B. J., Grant W. A. and Nobes M. J. (1972) Simulation study of lunar carbon chemistry. *Nat. Phys. Sci.* **235**, 108–109.
- Pizzarello S., Cooper G. W. and Flynn G. J. (2006) The nature and distribution of the organic material in carbonaceous chondrites and interplanetary dust particles. In *Meteorites and the Early Solar System II* (eds. D. S. Lauretta and J. H. Y. McSween). University of Arizona Press, Tucson, pp. 625–651.
- Ponnampuruma C., Kvenvolden K., Chang S., Johnson R., Pollock G., Philpott D., Kaplan I., Smith J., Schopf W. J., Gehrke C., Hodgson G., Brege I. A., Halpern B., Duffield A., Krauskopf K., Barghoorn E., Holland H. and Keil K. (1970) Search for organic compounds in the lunar dust from the sea of tranquility. *Science* **167**, 760–762.
- Preti G., Murphy R. C. and Biemann K. (1971) The search for organic compounds in various Apollo 12 samples by mass spectrometry. *Proc. Second Lunar Sci. Conf.*, 1879–1889.
- Reich S. and Thomsen C. (2004) Raman spectroscopy of graphite.. *Philos. Trans. R. Soc. A* **362**, 2271–2288.
- Robertson J. (2002) Diamond-like amorphous carbon. *Mater. Sci. Eng.* **R37**, 129–281.
- Sagan C. (1960) Indigenous organic matter on the Moon. *Proc. Natl. Acad. Sci.* **46**, 393–396.
- Sagan C. (1961) *Organic Matter and the Moon*. National Academy of Sciences Nation Research Council, Washington, DC.
- Sephton M. A. (2005) Organic matter in carbonaceous meteorites: past, present and future research. *R. Soc. London Philos. Trans. Ser. A* **363**, 2729–2742.
- Sephton M. A. and Gilmour I. (2000) Aromatic moieties in meteorites: relics of interstellar grain processes? *Astrophys. J.* **540**, 588–591.
- Shi Y. J. and Lipson R. H. (2005) An overview of organic molecule soft ionization using vacuum ultraviolet laser radiation. *Can. J. Chem.* **83**, 1891–1902.
- Steele A., McCubbin F. M., Fries M. D., Glamoclija M. and Nekvasil H. (2010) Graphite in an Apollo 17 Impact Melt Breccia. *Science* **329**, 51.
- Thomas K. L., Blanford G. E., Keller L. P., Klöck W. and McKay D. S. (1993) Carbon abundance and silicate mineralogy of anhydrous interplanetary dust particles. *Geochem. Cosmochim. Acta* **57**, 1551–1566.
- Tuinstra F. and Koenig J. L. (1970a) Raman scattering of graphite. *J. Compos. Mater.* **4**, 492–499.
- Tuinstra F. and Koenig J. L. (1970b) Raman spectrum of graphite. *J. Chem. Phys.* **53**, 1126–1130.
- Vanzani V., Marzari F. and Dotto E. (1997) Micrometeoroid impacts on the lunar surface. *Lunar Planet. Sci. Conf. XXVIII*, #1025.

- Warren P. and Haskin L. (1991) Lunar Chemistry. In *Lunar Sourcebook: A User's Guide to the Moon* (eds. G. H. Heiken, D. T. Vaniman and B. M. French). Cambridge University Press, New York, pp. 357–474.
- Weitz C. M., Rutherford M. J. and Head J. W. (1997) Oxidation states and ascent history of the Apollo 17 volcanic beads as inferred from metal-glass equilibria. *Geochim. Cosmochim. Acta* **61**, 2765–2775.
- Whittet D. C. B. (1997) Is extraterrestrial organic matter relevant to the origin of life on earth? In *Origins of Life and Evolution of the Biosphere* (ed. D. C. B. Whittet). Kluwer Academic Publishers, pp. 249–262.
- Zega T. J. and Stroud R. M. (2006) In situ lift-out with a focused ion beam/scanning electron microscope: a new technique for creating transmission electron microscope samples of natural and synthetic materials. *Proc. Scanning* **28**, 67–69.
- Zolensky M. E. (1997) Structural water in the Bench Crater chondrite returned from the Moon. *Meteorit. Planet. Sci.* **32**, 15–18.
- Zook H. A. (1975) The state of meteoritic material on the moon. *Proc. Lunar Sci. Conf.* **VI**, 1653–1672.

*Associate Editor:* Alexander Nemchin